Highly efficient large-area colourless luminescent solar concentrators using heavy-metal-free colloidal quantum dots

- Francesco Meinardi,
- Hunter McDaniel,
- Francesco Carulli,
- Annalisa Colombo,
- Kirill A. Velizhanin,
- Nikolay S. Makarov,
- Roberto Simonutti,
- Victor I. Klimov &
- Sergio Brovelli

Nature Nanotechnology **volume 10**, pages878–885(2015)Cite this article

- **3028** Accesses
- **288** Citations
- **159** Altmetric
- Metricsdetails

Abstract

Luminescent solar concentrators serving as semitransparent photovoltaic windows could become an important element in net zero energy consumption buildings of the future. Colloidal quantum dots are promising materials for luminescent solar concentrators as they can be engineered to provide the large Stokes shift necessary for suppressing reabsorption losses in large-area devices. Existing Stokes-shift-engineered quantum dots allow for only partial coverage of the solar spectrum, which limits their light-harvesting ability and leads to colouring of the luminescent solar concentrators, complicating their use in architecture. Here, we use quantum dots of ternary I–III–VI_2 semiconductors to realize the first large-area quantum dot–luminescent solar concentrators free of toxic elements, with reduced reabsorption and extended coverage of the solar spectrum. By incorporating $CuInSe_xS_{2-x}$ quantum dots into photo-polymerized poly(lauryl methacrylate), we obtain freestanding, colourless slabs that introduce no distortion to perceived colours and are thus well suited for the realization of photovoltaic windows. Thanks to the suppressed reabsorption and high emission efficiencies of the quantum dots, we achieve an optical power efficiency of 3.2%. Ultrafast spectroscopy studies suggest that the Stokes-shifted emission involves a conduction-band electron and a hole residing in an intragap state associated with a native defect.

Main

Building integrated photovoltaics has the potential to revolutionize future urban architecture by allowing the ambitious goal of net zero energy consumption buildings to be achieved. Luminescent solar concentrators (LSCs) could play an important role in this transition as they provide a mean to realize semitransparent photovoltaic windows that are able to convert the energy-passive facades of urban buildings into distributed energy generation units[1]. An LSC typically consists of a waveguide coated or doped with highly emissive chromophores. Direct and diffused sunlight is absorbed by the chromophores and re-emitted at a longer wavelength. The luminescence propagates to the waveguide edges by total internal reflection and is converted into electricity by photovoltaic cells installed along the slab perimeter (Fig. 1a)[1,2]. Because the surface area of the slab exposed to sunlight is much larger than the area of its edges, the LSC effectively increases the photon density incident onto the photovoltaic cell, which boosts its photocurrent[3]. Moreover, by matching the emission wavelength of active chromophores to the spectral peak of the external quantum efficiency (EQE), one can further increase the power output of photovoltaic devices[4]. It is also noteworthy that the colour and degree of transparency of an LSC, which are determined by the type and density of chromophores, can be chosen to meet specific building requirements and/or aesthetic criteria[1,5].

Figure 1: Concept of a reabsorption-free colourless LSC based on CISeS quantum dots.

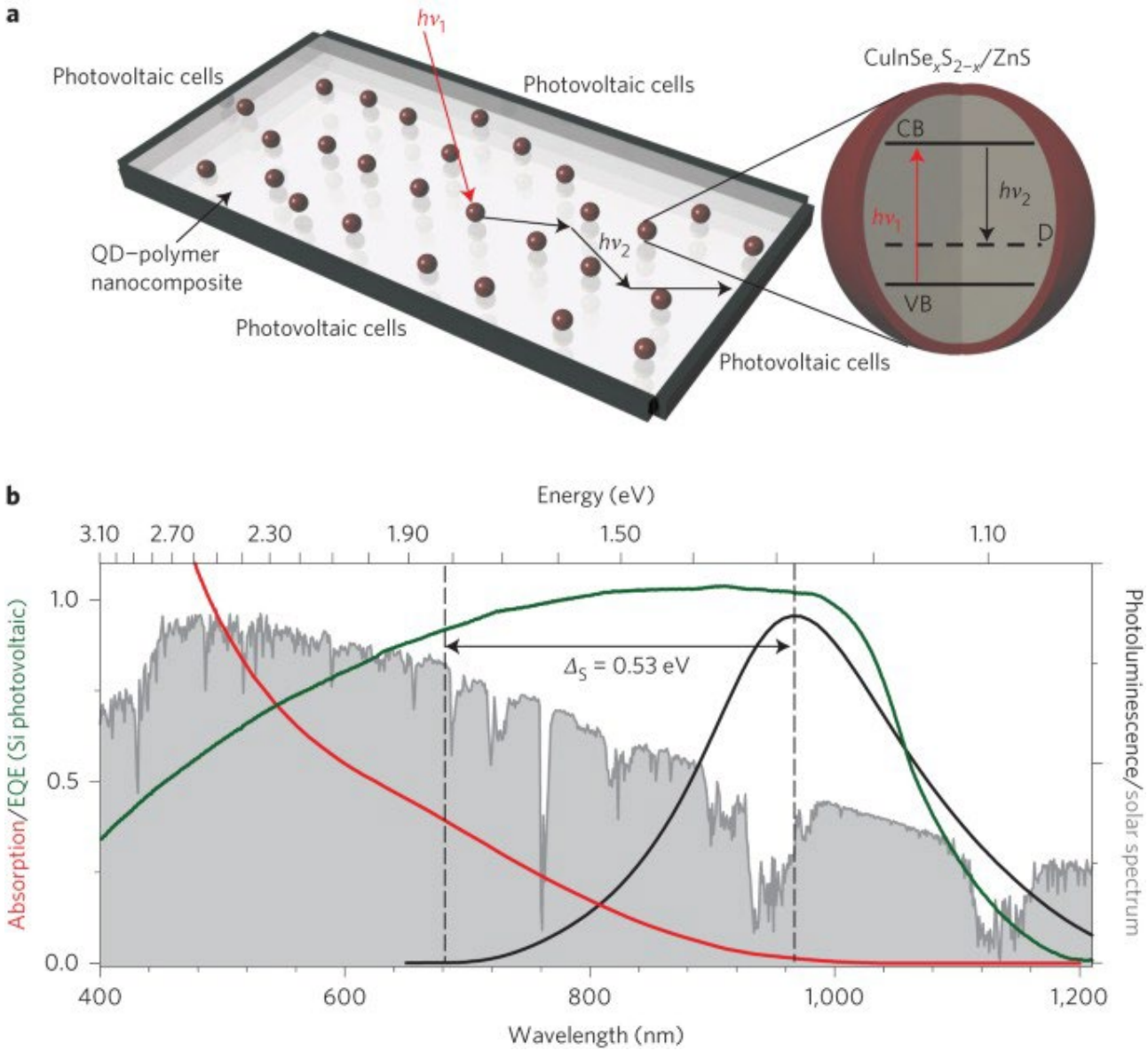

a, Schematic representation of a neutral-density LSC composed of a polymer matrix incorporating ZnS-coated CISeS quantum dots (QDs). A simplified structure of the band-edge electronic states in CISeS quantum dots responsible for light emission and absorption. Light absorption is dominated by optical transitions involving intrinsic quantized states (the valence and conduction bands are indicated as VB and CB respectively, the band-edge transition is shown by a red arrow) while emission (black arrow) involves a band-edge electron and an intragap hole state associated with a native defect (D) which results in a large Stokes shift. **b**, Absorption (red line) and photoluminescence (solid black line) spectra of ZnS-coated CISeS quantum dots in toluene. Photoluminescence was measured using c.w. excitation at 405 nm. The Stokes shift (indicated by a double-sided arrow) is 0.53 eV. The spectrum of solar radiation at sea level is shown by grey shading. The green line is the EQE curve of the 1 × 2.5 cm^2 c-Si photovoltaic cells used to build the concentrators, which are not optimized for maximum power conversion efficiency. Using high-performance photovoltaic cells with optimized design or high-end commercial modules will, in principle, allow the LSC efficiency to be increased further without introducing extra fabrication costs.

Full size image

Despite their promise, the wide use of LSCs has so far been hindered by a lack of suitable emitters. The typically used conjugated organic and organometallic fluorophores provide limited coverage of the solar spectrum, and suffer from significant optical losses associated with the reabsorption of guided luminescence[6,7,8,9] (Supplementary Fig. 1). These deficiencies reduce the light-harvesting efficiency of LSCs and also lead to strong colouring of devices, which imposes certain constraints on their use in architecture. Colloidal or nanocrystal quantum dots can help overcome these limitations[10,11,12,13,14]. They feature near-unity photoluminescence quantum yields (Φ_{PL}) and narrow, widely tunable emission spectra that can be matched to various solar cells including both single- and multi-junction devices. Most importantly for LSC applications, quantum dots can be engineered to provide a large Stokes shift, which allows the overlap between optical absorption and emission spectra to be greatly reduced, which is key to the realization of large-area LSCs with suppressed reabsorption losses[6]. Recently, several strategies to increase the Stokes shift have been demonstrated in the literature, including thick-shell CdSe/CdS heterostructures[15] and Mn-doped ZnSe quantum dots[16,17].

However, despite their great potential, LSCs fabricated using CdSe/CdS heterostructures or Mn-doped quantum dots suffer from incomplete coverage of the solar spectrum due to the large energy gap of the absorber material (2.46 eV for CdS and 2.7 eV for ZnSe), which may also lead to strong colouring of devices[15,18]. In the case of core/shell structures, this problem could be mitigated by using thick-shell PbSe/CdSe quantum dots, which feature a lowered absorption onset (~1.75 eV) and near-infrared luminescence in combination with a large effective Stokes shift[19,20]. These structures, however, contain hazardous heavy metal ions and thus require expensive disposal/recycling protocols, a problem similar to that encountered with CdSe/CdS nanocrystals.

An interesting class of non-toxic materials that provide a large, hundreds of meV Stokes shift without the need for heterostructuring are quantum dots of ternary I–III–VI_2 semiconductors such as $CuInS_2$ (CIS), $CuInSe_2$ (CISe) and their alloys ($CuInSe_xS_{2-x}$ or CISeS)[21,22,23,24]. An attractive feature of these quantum dots is that they do not contain heavy metals and can be fabricated in large quantities via high-throughput, non-injection techniques using inexpensive precursors[25]. Furthermore, their large absorption cross-sections and spectrally tunable, near-infrared absorption onset are well-suited for harvesting solar radiation[26]. They are also highly efficient tunable emitters, and their photoluminescence quantum yields can be pushed to above 80% using surface treatment with Cd^{2+} ions[27] or inorganic passivation with an outer shell of wide-gap ZnS[28].

Here, we use CISeS quantum dots coated with ZnS to realize the first highly efficient large-area infrared QD-LSC with reduced reabsorption losses and extended coverage of the solar spectrum. We focus on CISeS quantum dots with emission at 960 nm (1.3 eV),

which is near-optimal for LSCs coupled to Si photovoltaics and also allows for the realization of colourless quantum dot-doped slabs that are similar to neutral-density filters and therefore well-suited for applications as semitransparent windows.

Optical spectra of I–III–VI_2 quantum dots

The optical absorption and photoluminescence spectra of ZnS-coated CISeS quantum dots dissolved in toluene are reported in Fig. 1b, where they are compared to the terrestrial spectrum of solar radiation and a typical EQE spectrum of a Si photovoltaic cell. The absorption spectrum shows the almost featureless profile characteristic of ternary quantum dots[23] and extends over the entire range of visible wavelengths, which allows for efficient capture of solar radiation[29,30]. The photoluminescence spectrum closely matches the low-energy part of the EQE spectrum of a crystalline Si photovoltaic cell, which corresponds to a near-optimal situation for converting re-emitted photons into electrical current. The absorption spectrum exhibits a weak shoulder at ~640 nm (1.85 eV), which marks the position of the quantum dot band-edge. It is displaced from the photoluminescence band by 530 meV, which indicates a very large Stokes shift (Δ_S), greatly exceeding that of standard 'core-only' CdSe[15,31], PbS[32] or PbSe[33] quantum dots where it is typically a few tens of meV. An exceptionally large value of Δ_S is a general property of I–III–VI_2 quantum dots and is characteristic of both pure (CIS and CISe) and alloyed compositions[23,34,35]. The origin of the Stokes shift in I–III–VI_2 quantum dots is discussed in detail in the last section of this Article.

Polymer nanocomposites based on CISeS/ZnS quantum dots

We next focus on the chemistry of the incorporation of CISeS quantum dots into a transparent polymer matrix. To retain a high emission efficiency of the quantum dots during the encapsulation procedure, the emitting CISeS core is protected with a shell of wide-gap ZnS using the approach from ref. 27. Crosslinked poly(lauryl methacrylate) (PLMA) was used as a matrix material, as it has long side chains that prevent agglomeration of the quantum dots and allow for the fabrication of high-optical-quality quantum dot–polymer nanocomposites[11,17,36,37].

The chemical structures of the lauryl methacrylate monomer (LMA), ethylene glycol dimethacrylate (EGDM) crosslinker and IRGACURE 651 radical photoinitiator used in fabrication of the slabs are shown in Fig. 2a. Details of the nanocomposite photo-polymerization procedure are reported in the Methods. The high optical quality of the fabricated composites is illustrated by the photograph in Fig. 2b, which shows an LSC based on CISeS quantum dots and P(LMA-co-EGDM) with dimensions of 12 × 12 × 0.3 cm^3.

Figure 2: Quantum dot–polymer nanocomposites.

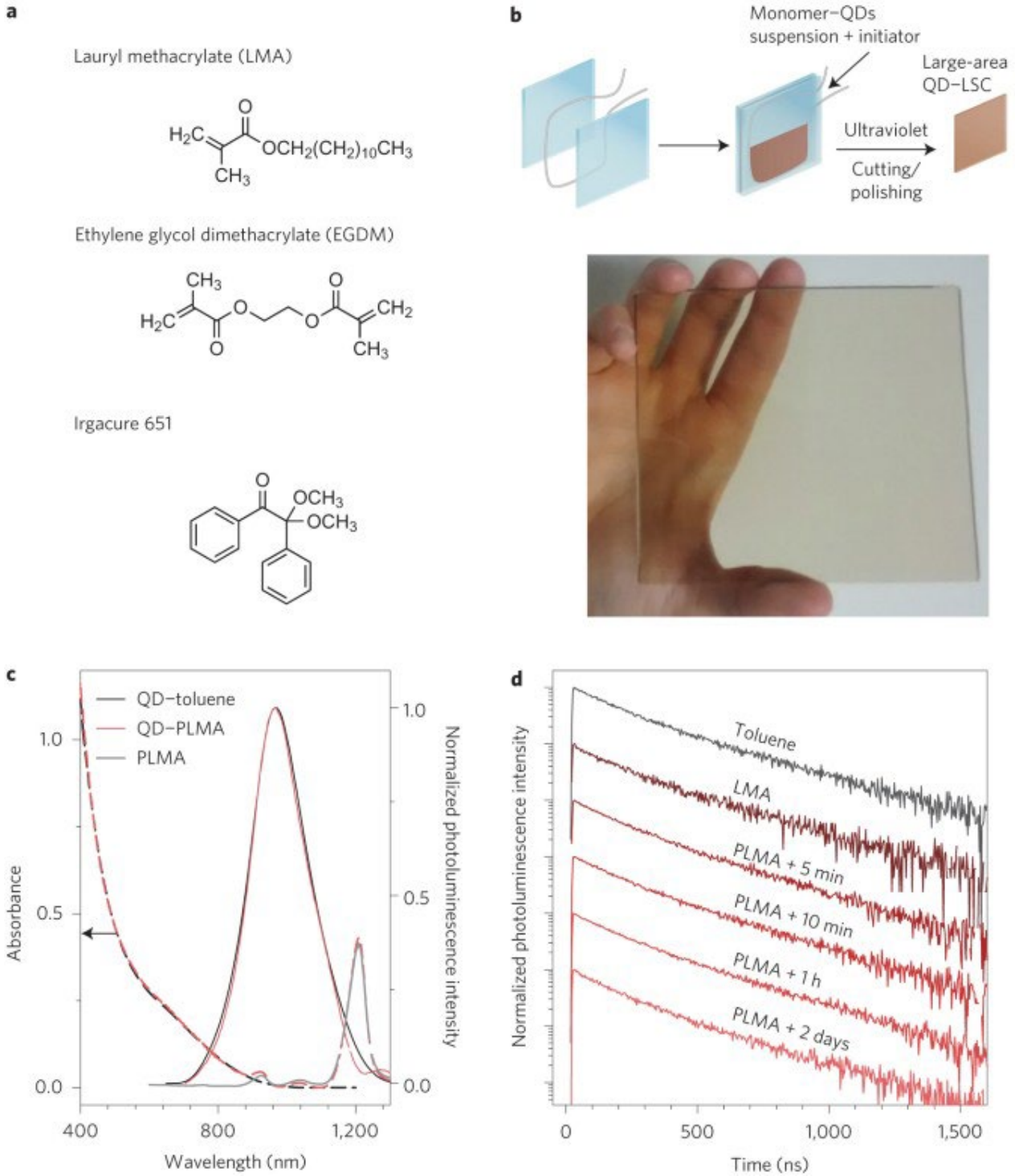

a, Chemical structure of organic precursors and a photoinitiator used for the fabrication of the polymer–quantum dot nanocomposites. **b**, Schematic representation of the cell casting procedure used for the fabrication of QD–LSCs (top) and a photograph of the LSC comprising 0.3 wt% quantum dots (by thermogravimetric analysis (TGA); Supplementary Fig. 3) under ambient illumination (bottom). LSC dimensions, $12 \times 12 \times 0.3$ cm^3. **c**, Absorption (dashed lines) and photoluminescence (solid lines) spectra of ZnS-coated CISeS quantum dots in toluene solution (black) and in photo-polymerized PLMA (pink). Photoluminescence was measured using c.w. excitation at 405 nm. The absorption spectrum of the P(LMA-co-EGDM) matrix is shown by a solid grey line. **d**, Photoluminescence decays measured using weak pulsed 405 nm excitation

of ZnS-coated CISeS quantum dots in different environments: toluene, LMA and (LMA-co-EGDM) matrix (at different times after completion of polymerization).

Full size image

Spectroscopic studies of the polymer nanocomposites revealed that the spectral and dynamical properties of ZnS-coated CISeS quantum dots are unaffected by the radical polymerization procedure. Specifically, both the absorption and photoluminescence spectra of the quantum dots in the polymer matrix are essentially identical to those of the quantum dots in toluene solution (Fig. 2c), and so is the photoluminescence quantum yield ($\Phi_{PL} = 40 \pm 4\%$). The absence of additional non-radiative decay channels in the nanocomposites was confirmed by photoluminescence decay measurements, which showed identical dynamics for the ZnS-coated quantum dots in toluene and in the LMA:EGDM:IRGACURE mixture before and after activation of the radical photocatalyst (Fig. 2d). In contrast, uncoated CISeS quantum dots undergo ~50% photoluminescence quenching upon activation of the radical catalyst (Supplementary Fig. 4).

High-efficiency large-area colourless LSCs

After characterizing the light-emitting properties of the nanocomposites, we proceeded to the analysis of optical losses due to reabsorption. To illustrate how the quantum dot photoluminescence is guided towards the slab edges, Figure 3a presents a photograph of one of the devices under ultraviolet illumination, taken with an ultraviolet-filtered infrared camera.

Figure 3: Experimental evaluation of reabsorption losses in LSCs based on CISeS quantum dots.

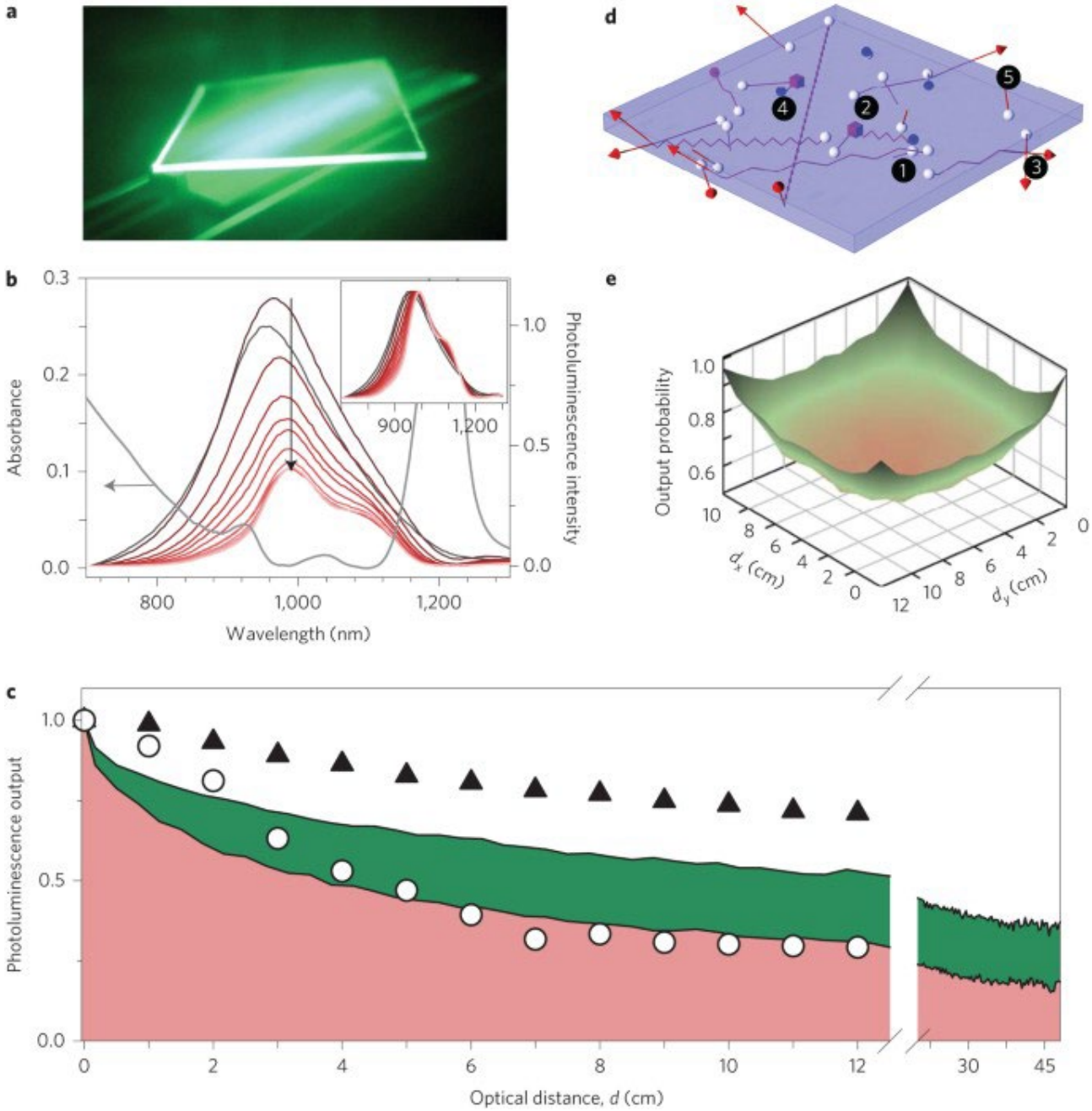

a, Photograph of an LSC comprising 0.3 wt% ZnS-coated CISeS quantum dots (concentrations measured by TGA, Supplementary Fig. 3; LSC dimensions, $12 \times 12 \times 0.3$ cm^3) taken with an ultraviolet-filtered infrared camera. The LSC is illuminated with ultraviolet light at 365 nm. **b**, Optical absorption spectrum (grey line) of the same LSC as in **a** and photoluminescence spectra (excitation at 532 nm) collected at the edge of the LSC when the excitation spot is located at an increasing distance (*d* from 0 to 12 cm) from the edge. The shape of the normalized photoluminescence spectra shows only a small change with *d* (inset), suggesting that losses to reabsorption are not significant. Non-normalized photoluminescence spectra (main panel) indicate that the overall photoluminescence intensity drops with increasing *d* due to scattering at optical imperfections within the P(LMA-co-EGDM) matrix and photon escape from the waveguide. **c**, Photoluminescence output as a function of *d* (circles; derived by integrating the spectra in the main panel of **b**) compared with the probability of a photon reaching the LSC edge computed using Monte Carlo ray tracing (shaded in pink

for $\Phi_{PL} = 40\%$ and in green for $\Phi_{PL} = 100\%$). The photoluminescence output obtained by integrating the normalized photoluminescence spectra in the inset of **b** is shown as black triangles. **d**, Examples of photon trajectories obtained using the Monte Carlo ray-tracing simulation: (1) the photon is created within the LSC via re-emission (white spheres); (2) the photon undergoes absorption/re-emission (purple cubes); (3) the photon reaches the device edge and is harvested by a photovoltaic cell (red arrows); (4) the photon is lost due to reabsorption followed by non-radiative decay (blues spheres); (5) the photon is lost by escaping through the top or the bottom surface of the device (red lines outside of the LSC). **e**, Map of relative probabilities for re-emitted photons reaching an LSC edge. The device contains 0.1 wt% ZnS-coated CISeS quantum dots, has dimensions of $12 \times 12 \times 0.3$ cm^3, and is exposed to uniform illumination from the top.

Full size image

Figure 3b shows the absorption spectrum of the quantum dot–polymer slab measured for light incident at a normal angle onto its largest side. The same figure also presents spectra of photoluminescence collected at one of the slab edges (12×0.3 cm^2) using continuous-wave (c.w.) 532 nm excitation with the pump spot positioned at different distances *d* from the sample edge. The photoluminescence intensity is observed to drop with increasing *d* (Fig. 3c) due to the combined effect of light escaping from the waveguide and reabsorption by the quantum dots and by the polymer matrix. To distinguish between the different mechanisms for optical losses, Monte Carlo ray-tracing simulations were carried out using the experimental parameters of the LSCs fabricated in this work (Fig. 3d,e) and neglecting scattering at optical imperfections within the slab or at its surfaces. The possible trajectories of photons generated inside the slab are depicted in Fig. 3d. The collection probability was also evaluated as a function of the lateral position of the point of origin of the emitted photon within the slab, considering uniform illumination of the LSC from the top (Fig. 3e). In these calculations we used the experimental absorption and emission profiles as well as the photoluminescence efficiency ($\Phi_{PL} = 40\%$) of the quantum dots embedded in the polymer waveguide (Fig. 2c). By averaging over 10^5–10^7 different emission events randomly generated across the device, the total output probability per originally emitted photon was calculated to be 44%, and the probabilities of a photon loss due to non-radiative decay following one or more reabsorption events or escape from the waveguide were 27% and 29%, respectively. To highlight the potential of our LSCs for the realization of large-area devices applicable as photovoltaic windows, Supplementary Fig. 5 reports the calculation of the output probability for devices up to 2×2 m^2. The simulation indicates that for $\Phi_{PL} = 40\%$, the output probability drops to ~50% of the output value for a 12×12 cm^2 slab for a 50-cm-wide waveguide, and for quantum dots with $\Phi_{PL} = 100\%$ the lateral slab size for 50% optical loss increases up to 1 m. To evaluate the role of losses due to scattering at optical imperfections, the results were modelled for experiments where photoluminescence was excited at different distances from the LSC edge (Fig. 3b). The simulated evolution of the photoluminescence intensity with *d* for the experimental photoluminescence quantum yield of 40% is shown in Fig. 3c. A fairly close correspondence between the modelling and the experimental data suggests that the

scattering losses disregarded by the model are indeed negligibly small in our devices. To estimate the ultimate optical power conversion efficiency achievable with these LSCs we modelled the situation where the quantum dot photoluminescence yield reaches the ideal value of 100% (Fig. 3c). In this case, the probability of harvesting a photon at the LSC edge increases to 61%, while the remaining 39% accounts for optical losses due to photon escape from the waveguide.

To distinguish losses due to reabsorption from those due to photon escape, the normalized photoluminescence spectra shown in the inset of Fig. 3b were analysed. In this case, the change in the photoluminescence signal can only occur as a result of spectral distortion caused by light reabsorption by the quantum dots and by the polymer matrix. Therefore, the spectrally integrated photoluminescence intensity can be used to quantify the emission losses due exclusively to reabsorption. Based on the plot in Fig. 3c, ~30% loss for a distance of 12 cm was estimated. This value is smaller than the attenuation observed, for example, for standard CdSe[15] of PbS[38] quantum dots, which is a direct consequence of the large Stokes shift characteristic of CISeS quantum dots. For comparison, standard PbS quantum dots with a Stokes shift of ~120 nm show more than 70% losses to reabsorption for a length of less than 8 cm (ref. 38).

To quantify the efficiency of the fabricated LSCs, the characterization set-up shown in Fig. 4a was used to study two samples that absorb 10% (LSC10, 0.3 wt% quantum dots, Fig. 4b) and 20% (LSC20, 0.5 wt% quantum dots, Fig. 4c) of the incident solar power. The concentrators were illuminated by a calibrated solar simulator (1.5 AM global). The light radiated from the edges of the waveguide was collected using calibrated Si photodiodes installed along the slab perimeter. To reproduce the situation of a photovoltaic window exposed to sunlight, no reflector was placed at the bottom of the slabs. Based on these measurements, optical power conversion efficiencies of $\eta = P_{out}/P_{in} = 1.02\%$ for LSC10 and $\eta = 3.27\%$ for LSC20 were obtained, where P_{out} is the luminous power collected by the photodiodes and P_{in} is the solar power incident onto the LSC. This result is particularly remarkable if one takes into account that both samples exhibit a high degree of transparency across the visible spectrum.

Figure 4: Colorimetry characterization of LSCs based on CISeS quantum dots.

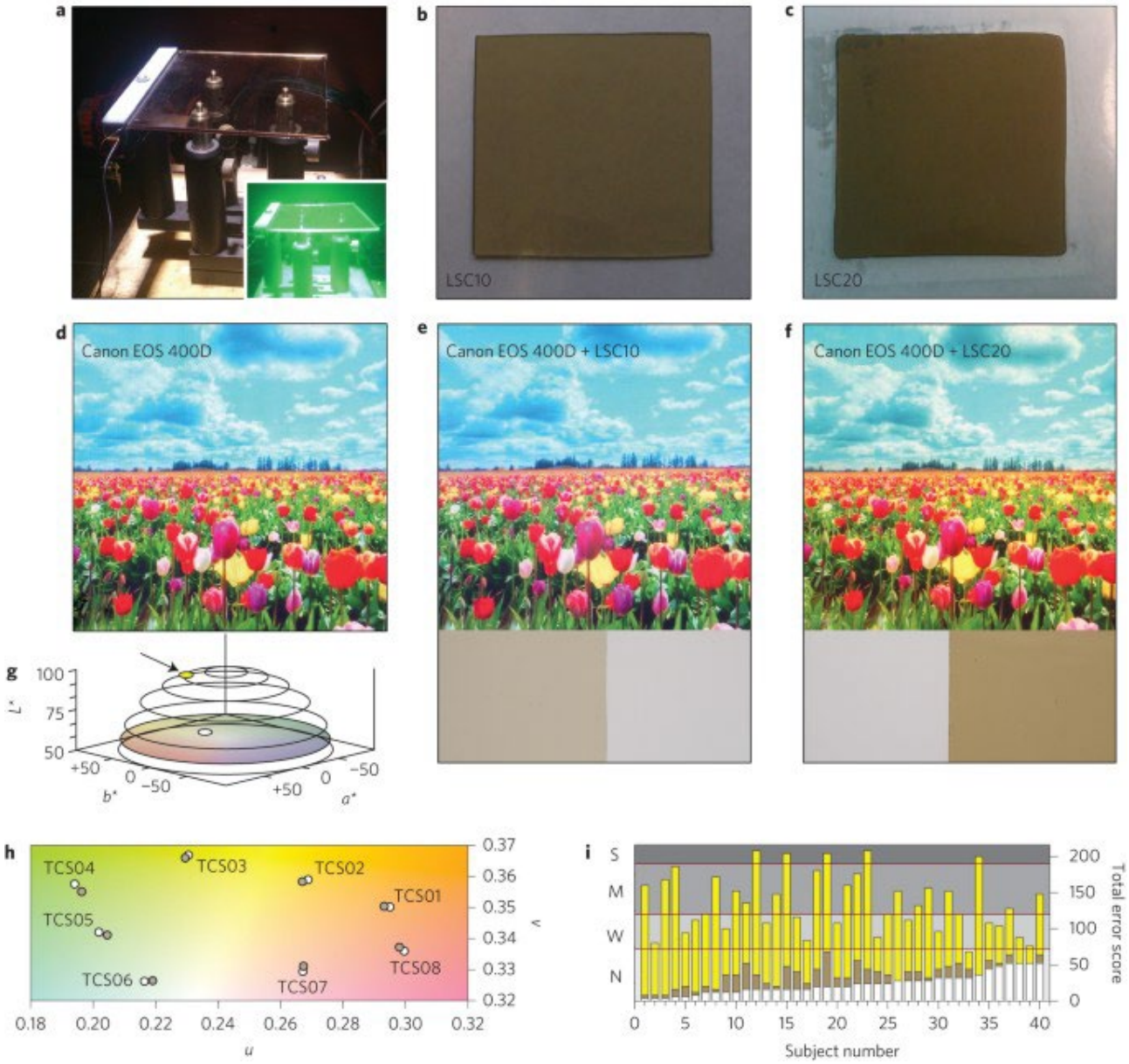

a, Photograph of a ZnS-coated CISeS QD–LSC during optical power conversion efficiency measurements with illumination from a solar simulator (1.5 AM global). Inset: photograph of the same device taken with an infrared camera. **b**,**c**, Photographs of large-area LSCs with dimensions of 12 × 12 × 0.3 cm^3 comprising 0.3 wt% quantum dots (LSC10) and 0.5 wt% quantum dots (LSC20) that absorb ∼10% and 20% of spectrally integrated incident radiation, respectively. **d**–**f**, Photographs of a colourful scene taken with a Canon EOS 400D camera without using any filters (**d**), or with LSC10 (**e**) or LSC20 (**f**) placed in front of the camera lens. To provide an estimate of the light attenuation effect in our devices, the lower panels report pictures of a reflecting white background taken with the same camera and filtering half of the field of view with LSC10 and LSC20, respectively. **g**, Colour coordinates in the CIE $L^*a^*b^*$ (Commission Internationale de le Éclairage) colour space of LSC20 (white circle, colour coordinates $L^* = 56.6$, $a^* = 5.1$ and $b^* = 32.1$), compared to a device based on Crs040 yellow organic dye (yellow circle, $L^* = 90.7$, $a^* = 3.3$ and $b^* = 55.3$). **h**, Colour coordinates (CIE 1960 Uniform Color Space) of original Munsell test colour samples (TCS) under D65 reference illuminant both unfiltered (white dots) and with spectral

filtering by LSC20 (brown dots). All coordinates with and without filter are very close to each other, resulting in a total colour rendering index of $R_a = 91$. **i**, Histogram of Farnsworth–Munsell 100 hue colour vision test performed on 40 normal subjects. The test was performed without colour filtering (white), and by filtering the subject's vision with LSC20 (brown) and with Crs040 LSC (yellow). Total error score, TES < 70, corresponds to normal chromatic vision (N), indicating no artificially induced colour blindness. Higher TES values correspond to strong alteration of the perceived colours, leading to weak (W), moderate (M) or severe (S) artificial colour blindness.

Full size image

Colorimetry analysis of LSCs based on I–III–VI_2 quantum dots

Another property of these LSCs, which benefits their application to building-integrated photovoltaics, is that they do not introduce a significant distortion to the spectrum of solar radiation; that is, they behave as uncoloured, neutral-density filters. This property is qualitatively illustrated in Fig. 4d–f, which presents photographs of a colour-rich scene taken either without any filtering or with LSC10 or LSC20 placed in front of the camera lens. Neither of the LSC samples introduces apparent colour distortions, and there is only a small effect from the denser LSC20 sample comprising a slight accentuation of warm colour tones.

To quantify the colour appearance of our devices and their effects on colour perception, and to further emphasize the difference with respect to traditional coloured LSCs, we performed colorimetry evaluations of LSC20 and of an LSC based on Radiant Crs040 Yellow, a typical large-Stokes-shift organic emitter (Supplementary Figs 1 and 6), fabricated so as to exhibit the same total absorptance across the whole solar spectrum (~20%)[39]. The colour of the LSCs was first evaluated using the CIE $L^*a^*b^*$ colour space, which is the conventional approach for assessing the appearance of materials under standard illumination[40]. The CIE $L^*a^*b^*$ coordinates of LSC20 are $L^* = 56.6$, $a^* = 5.1$ and $b^* = 32.1$, placing it in the dark brownish range of Munsell's colour atlas, which is a typical colouring of neutral sunglass lenses. In contrast, the LSC incorporating Crs040 has $L^* = 90.7$, $a^* = 3.3$ and $b^* = 55.3$, corresponding to Munsell brilliant yellow colour (Fig. 4g and Supplementary Fig. 7).

In addition to potentially imposing aesthetic constraints to the architectural applicability of LSC technology, colour plays a critical role as it determines the type and intensity of alteration of the colour perception LSCs might cause in individuals living in buildings with LSC-based photovoltaic windows. Partial absorption of the incident solar spectrum modifies the chromatic coordinates of natural sunlight and reduces its colour rendering index, resulting in altered colours of indoor settings. To quantify these effects, we measured both the CIE chromaticity coordinates and colour rendering index of sunlight after spectral filtration by either LSC20 or the Crs040-based LSC. The CIE coordinates

of D65 (noon daylight) reference illuminant transmitted through LSC20 are ($x = 0.45$, $y = 0.44$), close to the 2,650 K blackbody radiation of incandescent light bulbs. As expected, the corresponding analysis for Crs040-based LSC results instead in ($x = 0.47$, $y = 0.51$), corresponding to yellow light (Supplementary Fig. 8).

More importantly, the colour rendering analysis of LSC20 yields a colour rendering index of $R_a = 91$ (Fig. 4h) corresponding to CIE colour rendering group 1A, which fulfils the highest requirements for indoor illumination (typical applications: galleries, medical examination and colour mixing) and further confirms the colour neutrality of our LSCs. For direct comparison, the Crs040-based LSC has $R_a = 57$ (CIE group 3), suitable at best for industrial illumination (Supplementary Fig. 6).

LSCs could also modify the indoor-to-outdoor chromatic perception of individuals residing in buildings with LSC windows, with an effect analogous to artificially induced colour blindness. To evaluate this effect, a Farnsworth–Munsell 100 hue colour vision test was performed on 40 normal subjects[41,42]. To account for individual differences in colour sensitivity across the statistical population we repeated the test both without any filter and by filtering the subject's vision using LSC20 or Crs040 LSCs. The histogram of the total error score (TES) is reported in Fig. 4i. Using LSC20, all tested subjects obtained TES < 70 (median: $TES_{LSC20} = 38$ versus $TES_{No\ Filter} = 20$), corresponding to normal colour vision. In contrast, the Crs040 LSCs resulted in significant colour distortion ($TES_{Crs040} = 156$), leading to various degrees of induced colour blindness.

Origin of the large Stokes shift in I–III–VI_2 quantum dots

Finally, we discuss the origin of the large Stokes shift of ternary quantum dots. An important but still unanswered question is whether the observed energy separation is not just an ‘apparent’ but a ‘true’ Stokes shift. Indeed, looking at Figs 1–3, we note that the absorption spectrum does not fall off sharply past the peak on its low-energy side, but instead shows a long tail extending to the centre of the photoluminescence band. Such behaviour is typical of Si[43] and Ge[44] quantum dots or of type-II hetero-nanocrystals[45]. In these structures the band-edge transition is weak as it is indirect either in momentum or real space, which leads to the development of a large apparent Stokes shift defined by the energy spacing between the photoluminescence band and the first higher-energy strongly absorbing transition (typically, direct).

To investigate the light emission mechanism and the nature of a large Stokes shift in I–III–VI_2 quantum dots, we performed spectroscopic studies on quantum dots of pure CIS composition. In these quantum dots the wavelengths of both band-edge absorption and emission fall within the visible spectral range, which we can access experimentally using a combination of time-resolved photoluminescence and transient absorption techniques. Figure 5a reports the absorption and emission spectra of CIS quantum dots together with the photoluminescence excitation (PLE) spectrum. The photoluminescence band is centred at 600 nm (2.07 eV), and the first discernible absorption feature is at 500 nm (2.48 eV), corresponding to a Stokes shift of 410 meV. The PLE spectrum is

identical to the absorption spectrum, indicating that the photoluminescence is excited via intrinsic electronic transitions of the ternary semiconductor. We notice a small yet measurable shift of the PLE spectra collected on the blue and on the red tail of the photoluminescence spectrum (555 and 655 nm, Supplementary Fig. 9), which suggests that sample polydispersity contributes to the emission linewidth. To verify that the absorption shoulder does correspond to the band-edge transition, transient absorption studies were carried out. The measured transient absorption spectra are dominated by a bleaching band located exactly at the position of the absorption peak (~500 nm; Fig. 5b). At low excitation fluencies, when the number of photons absorbed per quantum dot per pulse ($\langle N \rangle$) is less than unity, this peak remains almost unchanged up to the longest pump–probe delays used in these measurements (~500 ps). This indicates that it is indeed due to saturation (Pauli blocking) of band-edge states where carriers accumulate following intraband relaxation. In the case of state filling, the transient absorption amplitude is proportional to the sum of the occupation factors of the electron and hole states involved in the optical transition. Because of the large hole effective masses and the complex multi-subband structure of the valence band, the density of hole states in I–III–VI_2 quantum dots is higher than that of the electron states. As a result, the single-state occupation factors of the valence-band levels are lower than those of the conduction-band levels, and hence the transient absorption amplitude is dominated by the contribution from the electrons. Thus, transient absorption studies confirm that the 500 nm (2.45 eV) feature observed in linear absorption marks the position of the quantum dot band-edge and hence a large separation between this feature and the photoluminescence band is a 'true' and not just an apparent Stokes shift. This further indicates that efficient emission from CIS quantum dots does not arise from the band-edge transition but rather is due to a radiative channel involving the band-edge electron level and an intragap hole state[23].

Figure 5: Origin of the Stokes shift in I–III–VI_2 quantum dots.

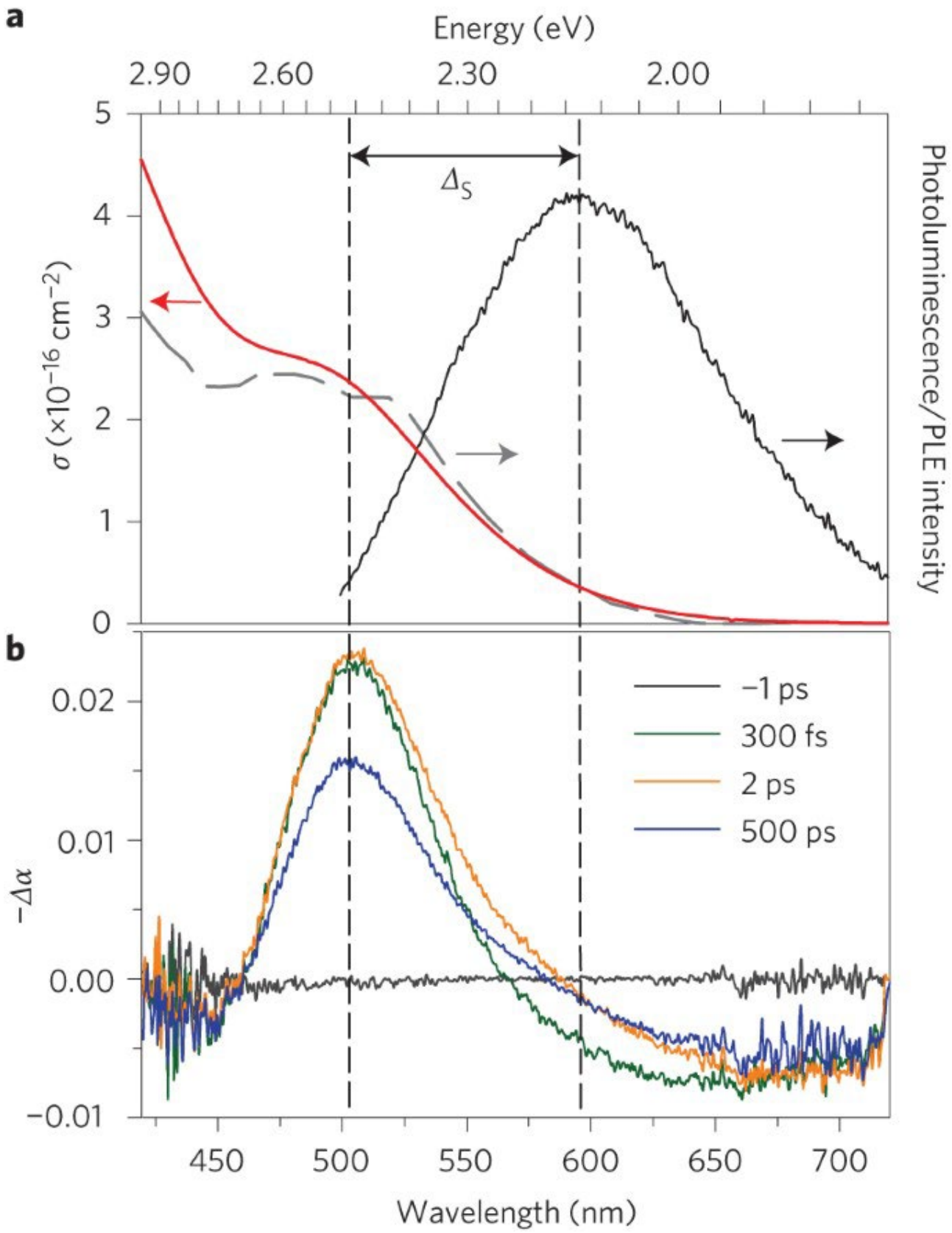

a, Absorption cross section σ (red line), photoluminescence (black line) and photoluminescence excitation (grey dashed line, detection wavelength 600 nm) spectra of 2 nm CIS quantum dots excited at 400 nm (3.1 eV). **b**, Transient absorption spectra ($-\Delta\alpha$) of the same quantum dots measured at different delays after excitation with 100 fs pump pulses at 3.1 eV, $\langle N \rangle = 0.7$.

Full size image

A survey of numerous literature reports suggests a remarkable consistency in the position of the photoluminescence band between CIS quantum dots prepared by different chemical approaches[22,25,29,34,35,41], which suggests that the hole-like defect responsible for intragap emission is native to this material system. One possibility indicated by recent magneto-photoluminescence studies[42] is that the intragap hole state is associated with the Cu^{2+} ion, which is a common substitutional impurity in II–VI semiconductors where it creates a fairly deep acceptor level[42,46,47]. In structural terms, I–III–VI_2 semiconductors are ternary analogues of II–VI materials, and their unit cell can be thought of as being composed of two zinc-blende unit cells distorted along the *c* axis. Therefore, it is reasonable to assume that substitutional Cu^{2+} impurities can also occur in I–III–VI_2 semiconductors. Based on charge balance considerations, one can think of two Cu^{2+} ions replacing Cu^{1+} and In^{3+} in adjacent sub-cells or Cu^{2+} paired with a Cu^{+1} vacancy, which is a well-known defect in bulk I–III–VI_2 materials[48].

Conclusions

We have demonstrated high-efficiency large-area LSCs with reduced reabsorption losses based on heavy-metal-free infrared-emitting I–III–VI_2 colloidal quantum dots in a mass polymerized plastic matrix. The optical transition responsible for light emission in these quantum dots involves an intragap hole state, which leads to a large Stokes shift and reduced losses to reabsorption. By over-coating quantum dots with a shell of wide-gap ZnS, their light emission properties are preserved during the entire process of their encapsulation into a polymer matrix. The use of these quantum dots allows us to overcome many limitations of both organic dyes and more traditional II–VI colloidal quantum dots (both undoped and doped), including strong colouring of the LSC and an incomplete coverage of the solar spectrum, which limits the light collection efficiency. As a result, we obtain an optical power conversion efficiency of up to 3.27%. Furthermore, our devices are essentially colourless and do not introduce any significant spectral distortion to transmitted sunlight or colour perception, which is beneficial for applications such as tinted photovoltaic windows.

Methods

Materials

LMA (99%, Aldrich) and EGDM (98%, Aldrich), purified with basic activated alumina (Sigma-Aldrich), were used as monomers for the preparation of polymer nanocomposites. IRGACURE 651 (Sigma-Aldrich) was used as a photoinitiator without purification. Crs040 yellow dye was purchased from Radiant Color NV.

Synthesis of quantum dots

The CIS and CISeS quantum dots used in this study were synthesized following the procedure described in ref. 29. Typically, copper (I) iodide and indium (III) acetate were

dissolved in a mixture of 1-dodecanethiol (DDT) and oleylamine (OLA) in a round-bottomed flask, and the mixture was degassed for 30 min. For CISeS, a solution of 1 M OLA/DDT-Se was made separately by mixing Se powder in OLA and DDT. The reaction flask was then heated to 230 °C for ~30 min, with OLA/DDT-Se added during heating for CISeS (otherwise, the reaction is roughly the same as for CIS). The resulting CISeS quantum dots were purified by iterative dissolution in chloroform and precipitation with methanol, and then stored in chloroform. For improved photoluminescence quantum yield and stability, the quantum dots were exposed to a solution of zinc oleate at elevated temperature, which formed a thin ZnS shell by cation exchange (as described in ref. 26).

Fabrication of nanocrystal–polymer composite

As the first step, a quantum dot powder was dispersed in a small volume of LMA monomer for 3 h to wet the nanoparticle surface and ensure fine dispersion of the individual quantum dots. The monomer–quantum dot mixture was then added to a large volume of LMA together with a secondary monomer, EGDM (LMA:EGDM 80:20% wt/wt), which acted as a crosslinking agent and a radical photoinitiator (IRGACURE 651; 1% wt/wt). After stirring the mixture for 20 min and sonication for 10 min to facilitate quantum dot dispersion, the homogeneous mixture was poured into a mould made of two low-roughness pieces of tempered glass linked by a poly(vinyl chloride) gasket, and irradiated with 365 nm light from a ultraviolet lamp for 5 min to trigger radical polymerization. The polymerization was then completed by keeping samples in the dark for 30 min while leaving them in the mould in order to avoid cracks. After completion of the procedure, the slabs were removed from the mould, cut into pieces of the desired sizes, and polished. The LSC based on Crs040 yellow dye was fabricated using the same protocol as used for the QD–LSCs.

Characterization of polymeric nanocomposite

Differential scanning calorimetry (DSC) measurements were performed using a Mettler Toledo STAR^{e} thermal analysis system. The thermal programme was characterized by three ramps: a first heating step from 0 °C to 200 °C at 10 °C min^{-1}, followed by a cooling step from 200 °C to 0 °C at −10 °C min^{-1}, and a final step of heating from 0 °C to 200 °C at 10 °C min^{-1}. During thermogravimetry measurements carried out using a transient absorption Q500 analyser (TA Instruments), samples were heated to 800 °C at 10 °C min^{-1} in air.

Spectroscopic studies

All spectroscopic studies were carried out using toluene solutions of quantum dots loaded into quartz cuvettes and quantum dot–PLMA nanocomposites. In the measurements of photoluminescence dynamics and transient absorption, the solution samples were vigorously stirred to avoid the effects of photocharging. Absorption spectra of quantum dot solutions and quantum dot–polymer composites were measured with a Perkin Elmer LAMBDA 950 UV/vis/NIR spectrophotometer.

Photoluminescence, PLE spectra and transient photoluminescence measurements were carried out using excitation with <70 ps pulses at 3.1 eV from a pulsed diode laser (Edinburgh Instruments EPL series). The emitted light was collected with a liquid-nitrogen-cooled low-noise Hamamatsu NIR (R5509-73) photomultiplier tube (PMT) coupled to time-correlated single-photon-counting (TCSPC) electronics (time resolution of ∼150 ps). Optical measurements on LSCs were carried out by coupling the output edge of the slab to an integrating sphere and using a 532 nm c.w. laser as an excitation source. The photoluminescence was detected with the same PMT and TCSPC unit. The same set-up was used for photoluminescence quantum yield measurements.

Transient absorption measurements were performed on quantum dots of pure CIS composition. In these quantum dots, the wavelengths of both band-edge absorption and emission fall within the visible spectral range, which we can access experimentally by using a combination of time-resolved photoluminescence and transient absorption techniques. The analysis conducted for CIS quantum dots should be applicable to CISeS quantum dots of arbitrary formulations, as the main effect of the incorporation of Se is a lowering of photoluminescence and absorption energies as a result of the reduced bandgap. Measurements were carried out using a LabView-controlled home-built set-up in a standard pump–probe configuration with 400 nm, ∼100 fs pump pulses (1 kHz repetition rate) and a broadband, white-light supercontinuum probe. The excitation spot diameter was 800 μm at the $1/e^2$ level. The measurements were performed on quantum dot solutions with an optical density (OD) below 2 at 400 nm, corresponding to quantum dot concentrations of less than 1×10^{-5} M. All spectroscopic measurements were conducted under oxygen-free and moisture-free conditions using air-tight quartz cuvettes. The organic solvents were dry and stored under argon. Sample preparation was performed in an inert atmosphere in a glovebox.

Monte Carlo ray-tracing simulation

Theoretical analysis of the efficiency of the LSC was performed using a Monte Carlo ray-tracing method[49], in which propagation of a photon within the LSC was modelled as propagation of a geometrical ray subject to refraction/reflection at the air–LSC interfaces according to Fresnel laws. Accordingly, no interference was taken into account. The stochastic nature of the simulations is reflected in the fact that the ray is not split upon reaching an interface but is instead transmitted or reflected, with probabilities proportional to the respective energy fluxes given by the Fresnel laws. The dependence of these probabilities on the state of polarization of the incident ray (for example, *s*- or *p*-polarized) is also taken into account. A specific event (that is, transmission or reflection) is chosen according to random Monte Carlo drawing.

Monte Carlo ray-tracing simulations were performed using the experimental photoluminescence spectrum and efficiency ($\Phi_{PL} = 40\%$) of the quantum dots embedded in the polymer waveguide. Furthermore, the absorption spectrum of the polymer slab doped with quantum dots was used to account also for absorption by the polymer matrix.

Inside the LSC material, for each ray, the inverse transform sampling method was applied to randomly generate the length of the optical path before absorption by quantum dots. Path lengths followed the exponential attenuation law determined by the wavelength-dependent absorption cross-section $\sigma(\lambda)$ and the quantum dot concentration N_{QD}, via an attenuation coefficient, $k(\lambda) = N_{QD}\sigma(\lambda)$. Because the mean path length, given by the inverse attenuation coefficient, is always much greater than the average distance between quantum dots, there is no need to keep track of the explicit position of each quantum dot, so the LSC material (PLMA + quantum dots) can be considered to fall within the effective medium approach (that is, it is a uniform material with the attenuation coefficient defined above).

Once a photon is absorbed by a quantum dot, the subsequent fate of the excitation (that is, re-emission or non-radiative relaxation) is again determined by the Monte Carlo sampling according to the photoluminescence quantum yield. The direction of re-emission is distributed uniformly and the re-emission wavelength is determined using the rejection sampling applied to the accurate quantum dot photoluminescence spectrum obtained from experiment.

The ultimate fate of each photon is either loss due to non-radiative recombination or escape from the LSC via one of the interfaces. A single-ray Monte Carlo simulation is typically repeated 10^5–10^7 times to achieve proper statistical averaging. The stochastic nature of simulations allows one to easily evaluate various observables and add additional processes.

Colorimetry studies

CIE $L^*a^*b^*$ colour coordinates were extracted from the reflectance spectra measured with a Perkin Elmer Lambda 9000 spectrometer, using an integrating sphere and placing a Spectralon scatterer on the back side of the LSCs, following the conventional procedure for colorimetric measurements on semitransparent materials. Both diffused and reflected light (8°) were collected. The D65 illuminant spectrum was used for calculation of the L^*, a^* and b^* coordinates.

The colour rendering index of the light transmitted by the LSCs was calculated following the CIE13.3 procedure using eight Munsell test colour samples (TCSs). The D65 illuminant spectrum was used as the light source, either as a reference or filtered by the experimental absorption spectra of the LSCs.

The Farnsworth–Munsell 100 hue colour vision test is commonly used to measure an individual's colour vision acuity by probing the ability to discriminate tiny differences in a set of colour targets with constant value and chroma, covering all the visual hues described by the Munsell colour system. In this Article, we used a typical version of the F-M100 Hue Test, which is based on four distinct rows of targets with similar colour hues, each containing 25 distinct variations of each hue. Each colour hue at the extreme

of a row is fixed in position (anchor targets) and subjects are asked to arrange the other targets so as to form a gradual transition in chroma between the two anchor targets. The final arrangement of the hue targets represents the aptitude of the visual system in discerning differences in colour hue. Failures within the observer's visual system are measured by considering both the amount of instances that a target is misplaced, or the severity of a target displacement (that is, the distance between where a target should have been placed and where it was actually placed). These factors are summarized in a so-called total error score (TES), which quantifies the colour impairment of a subject, or, in normal subjects, can be used as in indicator of the artificial colour blindness induced by coloured filters (that is, glass lenses, coloured windows). The test was performed on 40 subjects without congenital colour impairment (normal subject) between 20 and 55 years of age. To account for individual differences in colour sensitivity across the statistical population, for each subject the test was performed under identical conditions both without any filter and by filtering the subject's vision using the LSCs. The chronological order of tests for the three conditions (no filter, LSC20 and Crs040 LSC) was chosen randomly across the population to avoid the results being biased by learning effects. The test was conducted on a calibrated monitor (Dell Vostro 3750).

References

1. 1

   Debije, M. G. & Verbunt, P. P. C. Solar concentrators: thirty years of luminescent solar concentrator research: solar energy for the built environment. *Adv. Energ. Mater*. **2**, 12–35 (2012).

   CAS **Article** **Google Scholar**

2. 2

   Currie, M. J., Mapel, J. K., Heidel, T. D., Goffri, S. & Baldo, M. A. High-efficiency organic solar concentrators for photovoltaics. *Science* **321**, 226–228 (2008).

   CAS **Article** **Google Scholar**

3. 3

   Rau, U., Einsele, F. & Glaeser, G. C. Efficiency limits of photovoltaic fluorescent collectors. *Appl. Phys. Lett*. **87**, 171101 (2005).

   Article **Google Scholar**

4. 4

Van Sark, W. G. J. H. M. et al. Luminescent solar concentrators—a review of recent results. *Opt. Express* **16**, 21773–21792 (2008).

CAS **Article** **Google Scholar**

5. 5

Zhao, Y., Meek, G. A., Levine, B. G. & Lunt, R. R. Near-infrared harvesting transparent luminescent solar concentrators. *Adv. Opt. Mater*. **2**, 606–611 (2014).

CAS **Article** **Google Scholar**

6. 6

Giebink, N. C., Wiederrecht, G. P. & Wasielewski, M. R. Resonance-shifting to circumvent reabsorption loss in luminescent solar concentrators. *Nature Photon*. **5**, 694–701 (2011).

CAS **Article** **Google Scholar**

7. 7

Desmet, L., Ras, A. J. M., de Boer, D. K. G. & Debije, M. G. Monocrystalline silicon photovoltaic luminescent solar concentrator with 4.2% power conversion efficiency. *Opt. Lett*. **37**, 3087–3089 (2012).

CAS **Article** **Google Scholar**

8. 8

Wang, T. et al. Luminescent solar concentrator employing rare earth complex with zero self-absorption loss. *Sol. Energy* **85**, 2571–2579 (2011).

CAS **Article** **Google Scholar**

9. 9

Debije, M. G. et al. Promising fluorescent dye for solar energy conversion based on a perylene perinone. *Appl. Opt*. **50**, 163–169 (2011).

CAS **Article** **Google Scholar**

10. 10

Krumer, Z. et al. Tackling self-absorption in luminescent solar concentrators with type-II colloidal quantum dots. *Sol. Energy Mater. Sol. Cell* **111**, 57–65 (2013).

CAS **Article** **Google Scholar**

11. 11

Bomm, J. et al. Fabrication and full characterization of state-of-the-art quantum dot luminescent solar concentrators. *Sol. Energy Mater. Sol. Cell*. **95**, 2087–2094 (2011).

CAS **Article** **Google Scholar**

12. 12

Chatten, A. J., Barnham, K. W. J., Buxton, B. F., Ekins-Daukes, N. J. & Malik, M. A. Quantum dot solar concentrators. *Semiconductors* **38**, 909–917 (2004).

CAS **Article** **Google Scholar**

13. 13

Gallagher, S. J., Norton, B. & Eames, P. C. Quantum dot solar concentrators: electrical conversion efficiencies and comparative concentrating factors of fabricated devices. *Sol. Energy* **81**, 813–821 (2007).

CAS **Article** **Google Scholar**

14. 14

Purcell-Milton, F. & Gun'ko, Y. K. Quantum dots for luminescent solar concentrators. *J. Mater. Chem*. **22**, 16687–16697 (2012).

CAS **Article** **Google Scholar**

15. 15

Meinardi, F. et al. Large area luminescent solar concentrators based on ‘Stokes-shift-engineered’ nanocrystals in a mass polymerized PMMA matrix. *Nature Photon*. **8**, 392–399 (2014).

CAS **Article** **Google Scholar**

16. 16

Bradshaw, L. R., Knowles, K. E., McDowall, S. & Gamelin, D. R. Nanocrystals for luminescent solar concentrators. *Nano Lett*. **15**, 1315–1323 (2015).

CAS **Article** **Google Scholar**

17. 17

Erickson, C. S. et al. Zero-reabsorption doped-nanocrystal luminescent solar concentrators. *ACS Nano* **8**, 3461–3467 (2014).

CAS **Article** **Google Scholar**

18. 18

Coropceanu, I. & Bawendi, M. G. Core/shell quantum dot based luminescent solar concentrators with reduced reabsorption and enhanced efficiency. *Nano Lett*. **14**, 4097–4101 (2014).

CAS **Article** **Google Scholar**

19. 19

Cirloganu, C. M. et al. Enhanced carrier multiplication in engineered quasi-type-II quantum dots. *Nature Commun.* **5**, 4148 (2014).

CAS **Article** **Google Scholar**

20. 20

Lin, Q. et al. Design and synthesis of heterostructured quantum dots with dual emission in the visible and infrared. *ACS Nano* **9**, 539–547 (2015).

CAS **Article** **Google Scholar**

21.21

Aldakov, D., Lefrancois, A. & Reiss, P. Ternary and quaternary metal chalcogenide nanocrystals: synthesis, properties and applications. *J. Mater. Chem. C* **1**, 3756–3776 (2013).

CAS **Article** **Google Scholar**

22.22

Kolny-Olesiak, J. & Weller, H. Synthesis and application of colloidal CuInS2 semiconductor nanocrystals. *ACS Appl. Mater. Interfaces* **5**, 12221–12237 (2013).

CAS **Article** **Google Scholar**

23.23

Li, L. et al. Efficient synthesis of highly luminescent copper indium sulfide-based core/shell nanocrystals with surprisingly long-lived emission. *J. Am. Chem. Soc*. **133**, 1176–1179 (2011).

CAS **Article** **Google Scholar**

24.24

Akkerman, Q. A. et al. From binary Cu2S to ternary Cu–In–S and quaternary Cu–In–Zn–S nanocrystals with tunable composition via partial cation exchange. *ACS Nano* **9**, 521–531 (2015).

CAS **Article** **Google Scholar**

25.25

Zhong, H. et al. Noninjection gram-scale synthesis of monodisperse pyramidal CuInS2 nanocrystals and their size-dependent properties. *ACS Nano* **4**, 5253–5262 (2010).

CAS **Article** **Google Scholar**

26.26

McDaniel, H., Fuke, N., Makarov, N. S., Pietryga, J. M. & Klimov, V. I. An integrated approach to realizing high-performance liquid-junction quantum dot sensitized solar cells. *Nature Commun.* **4**, 2887 (2013).

Article **Google Scholar**

27.27

McDaniel, H., Fuke, N., Pietryga, J. M. & Klimov, V. I. Engineered CuInSe*x*S2–*x* quantum dots for sensitized solar cells. *J. Chem. Phys. Lett*. **4**, 355–361 (2013).

CAS **Article** **Google Scholar**

28.28

Yarema, O. et al. Highly luminescent, size- and shape-tunable copper indium selenide based colloidal nanocrystals. *Chem. Mater*. **25**, 3753–3757 (2013).

CAS **Article** **Google Scholar**

29.29

McDaniel, H. et al. Simple yet versatile synthesis of CuInSe*x*S2–*x* quantum dots for sunlight harvesting. *J. Phys, Chem. C* **118**, 16987–16994 (2014).

CAS **Article** **Google Scholar**

30.30

Panthani, M. G. et al. Synthesis of CuInS2, CuInSe2, and Cu(In*x*Ga1–*x*)Se2 (CIGS) nanocrystal 'inks' for printable photovoltaics. *J. Am. Chem. Soc*. **130**, 16770–16777 (2008).

CAS **Article** **Google Scholar**

31.31

García-Santamaría, F. et al. Breakdown of volume scaling in Auger recombination in CdSe/CdS heteronanocrystals: the role of the core–shell interface. *Nano Lett*. **11**, 687–693 (2011).

Article **Google Scholar**

32.32

Stewart, J. T. et al. Comparison of carrier multiplication yields in PbS and PbSe nanocrystals: the role of competing energy-loss processes. *Nano Lett*. **12**, 622–628 (2011).

Article **Google Scholar**

33.33

Semonin, O. E. et al. Absolute photoluminescence quantum yields of IR-26 dye, PbS, and PbSe quantum dots. *J. Chem. Phys. Lett*. **1**, 2445–2450 (2010).

CAS **Article** **Google Scholar**

34.34

Chen, B. et al. Highly emissive and color-tunable CuInS2-based colloidal semiconductor nanocrystals: off-stoichiometry effects and improved electroluminescence performance. *Adv. Funct. Mater*. **22**, 2081–2088 (2012).

CAS **Article** **Google Scholar**

35.35

De Trizio, L. et al. Strongly fluorescent quaternary Cu–In–Zn–S nanocrystals prepared from Cu1–*x*InS2 nanocrystals by partial cation exchange. *Chem. Mater*. **24**, 2400–2406 (2012).

CAS **Article** **Google Scholar**

36.36

Bomm, J. et al. Fabrication and spectroscopic studies on highly luminescent CdSe/CdS nanorod polymer composites. *Beilstein J. Nanotechnol*. **1**, 94–100 (2010).

CAS **Article** **Google Scholar**

37.37

Bronstein, N. D. et al. Luminescent solar concentration with semiconductor nanorods and transfer-printed micro-silicon solar cells. *ACS Nano* **8**, 44–53 (2013).

Article **Google Scholar**

38.38

Shcherbatyuk, G. V., Inman, R. H., Wang, C., Winston, R. & Ghosh, S. Viability of using near infrared PbS quantum dots as active materials in luminescent solar concentrators. *Appl. Phys. Lett*. **96**, 191901 (2010).

Article **Google Scholar**

39.39

Slooff, L. H. et al. A luminescent solar concentrator with 7.1% power conversion efficiency. *Phys. Status Solidi Rapid Res. Lett*. **2**, 257–259 (2008).

CAS **Article** **Google Scholar**

40.40

Hunter, R. S. Photoelectric color-difference meter. *J. Opt. Soc. Am.* **38**, 985–993 (1948).

Google Scholar

41.41

Witt, E. & Kolny-Olesiak, J. Recent developments in colloidal synthesis of CuInSe2 nanoparticles. *Chem. Eur. J.* **19**, 9746–9753 (2013).

CAS **Article** **Google Scholar**

42.42

Rice, W. D., McDaniel, H., Klimov, V. I. & Crooker, S. A. Magneto-optical properties of CuInS2 nanocrystals. *J. Chem. Phys. Lett*. **5**, 4105–4109 (2014).

CAS **Article** **Google Scholar**

43.43

Meier, C., Gondorf, A., Lüttjohann, S., Lorke, A. & Wiggers, H. Silicon nanoparticles: absorption, emission, and the nature of the electronic bandgap. *J. Appl. Phys*. **101**, 103112 (2007).

Article **Google Scholar**

44.44

Lee, D. C. et al. Colloidal synthesis of infrared-emitting germanium nanocrystals. *J. Am. Chem. Soc*. **131**, 3436–3437 (2009).

CAS **Article** **Google Scholar**

45.45

Kim, S., Fisher, B., Eisler, H.-J. & Bawendi, M. Type-II quantum dots: CdTe/CdSe(core/shell) and CdSe/ZnTe(core/shell) heterostructures. *J. Am. Chem. Soc*. **125**, 11466–11467 (2003).

CAS **Article** **Google Scholar**

46.46

Viswanatha, R., Brovelli, S., Pandey, A., Crooker, S. A. & Klimov, V. I. Copper-doped inverted core/shell nanocrystals with 'permanent' optically active holes. *Nano Lett*. **11**, 4753–4758 (2011).

CAS **Article** **Google Scholar**

47.47

Pandey, A. et al. Long-lived photoinduced magnetization in copper-doped ZnSe–CdSe core–shell nanocrystals. *Nature Nanotech*. **7**, 792–797 (2012).

CAS **Article** **Google Scholar**

48.48

Binsma, J. J. M., Giling, L. J. & Bloem, J. Luminescence of CuInS2: I. The broad band emission and its dependence on the defect chemistry. *J. Lumin*. **27**, 35–53 (1982).

CAS Article Google Scholar

49.49

Şahin, D., Ilan, B. & Kelley, D. F. Monte-Carlo simulations of light propagation in luminescent solar concentrators based on semiconductor nanoparticles. *J. Appl. Phys*. **110**, 033108 (2011).

Article Google Scholar

Download references

Acknowledgements

S.B. and F.M. acknowledge support from the Cariplo Foundation (2012-0844). V.I.K., H.M., K.A.V. and N.S.M. were supported by the Center for Advanced Solar Photophysics (CASP), an Energy Frontier Research Center funded by the Office of Basic Energy Sciences, Office of Science, US Department of Energy. S.B. acknowledges financial support from the European Community's Seventh Framework Programme (FP7/2007–2013) under grant agreement no. 324603 (EDONHIST). The authors thank M. Acciarri and the staff of the MIB-SOLAR laboratory for technical assistance in the quantitative studies of solar concentration and L. Raimondo and V. Pinchetti for assistance with the colorimetric analysis.